Icarus 387 (2022) 115179

Contents lists available at ScienceDirect

Icarus

journal homepage: www.elsevier.com/locate/icarus

The power of paired proximity science observations: Co-located data from SHERLOC and PIXL on Mars

Joseph Razzell Hollis [a,b,*], Kelsey R. Moore [a,c,*], Sunanda Sharma [a], Luther Beegle [a], John P. Grotzinger [c], Abigail Allwood [c], William Abbey [a], Rohit Bhartia [d], Adrian J. Brown [e], Benton Clark [f], Edward Cloutis [g], Andrea Corpolongo [h], Jesper Henneke [i], Keyron Hickman-Lewis [b,j], Joel A. Hurowitz [k], Michael W.M. Jones [l], Yang Liu [a], Jesús Martinez-Frías [m], Ashley Murphy [n], David A.K. Pedersen [i], Svetlana Shkolyar [o,p], Sandra Siljeström [q], Andrew Steele [r], Mike Tice [s], Alan Treiman [t], Kyle Uckert [a], Scott VanBommel [u], Anastasia Yanchilina [v]

[a] NASA Jet Propulsion Laboratory, California Institute of Technology, Pasadena, CA, USA
[b] The Natural History Museum, London, UK
[c] California Institute of Technology, Pasadena, CA, USA
[d] Photon Systems Inc., Covina, CA, USA
[e] Plancius Research, Severna Park, MD, USA
[f] Space Science Institute, Boulder, CO, USA
[g] C-TAPE, University of Winnipeg, Winnipeg, Manitoba, Canada
[h] Department of Geology, University of Cincinnati, Cincinnati, OH, USA
[i] Technical University of Denmark, DTU Space, Division of Measurement and Instrumentation Systems, Kongens Lyngby, Denmark
[j] Dipartimento di Scienze Biologiche, Geologiche e Ambientali, Università di Bologna, Bologna, Italy
[k] Department of Geosciences, Stony Brook University, Stony Brook, NY, USA
[l] Central Analytical Research Facility & School of Chemistry and Physics, Queensland University of Technology, Brisbane, Australia
[m] Institute of Geosciences, Consejo Superior de Investigaciones Científicas (CSIC-UCM), Madrid, Spain
[n] Planetary Science Institute, Tucson, AZ, USA
[o] Department of Astronomy, University of Maryland, College Park, MD, USA
[p] Planetary Geology, Geophysics and Geochemistry Lab, NASA Goddard Space Flight Center, Greenbelt, MD, USA
[q] Department of Methodology, Textiles and Medical Technology, RISE Research Institutes of Sweden, Stockholm, Sweden
[r] Earth and Planets Laboratory, Carnegie Institution for Science, Washington DC, USA
[s] Department of Geology & Geophysics, Texas A&M University, TX, USA
[t] Lunar and Planetary Institute, Universities Space Research Association, Houston, TX, USA
[u] Washington University in St. Louis, St. Louis, MO, USA
[v] Impossible Sensing LLC, St. Louis, MO, USA

A B S T R A C T

We present a synthesis of PIXL elemental data and SHERLOC Raman spectra collected on two targets investigated by the *Perseverance* rover during the first year of its exploration of Jezero Crater, Mars. The Bellegarde target (in the Máaz formation) and Dourbes target (in the Séítah formation) exhibit distinctive mineralogies that are an ideal case study for in situ analysis by SHERLOC and PIXL. Each instrument alone produces valuable data about the chemistry and spatial distribution of mineral phases at the sub-millimeter scale. However, combining data from both instruments provides a more robust interpretation that overcomes the limitations of either instrument, for example: 1) Detection of correlated calcium and sulfur in Bellegarde by PIXL is corroborated by the co-located detection of calcium sulfate by SHERLOC. 2) Detection of sodium and chlorine in Dourbes is consistent with either chloride or oxychlorine salts, but SHERLOC does not detect perchlorate or

Abbreviations: ACI, Autofocus Context Imager; CCD, Charge-Coupled Device; DUV, Deep Ultraviolet; gDRT, gas Dust Removal Tool; HDR, High Dynamic Range; MCC, Micro-Context Camera; NIRVIS, Near-Infrared Visible; PIXL, Planetary Instrument for X-ray Lithochemistry; ROI, Region of Interest; SHERLOC, Scanning Habitable Environments with Raman and Luminescence for Organics and Chemicals; XRF, X-Ray Fluorescence; WATSON, Wide-Angle Topographic Sensor for Operations and eNgineering.

* Corresponding authors at: NASA Jet Propulsion Laboratory, California Institute of Technology, Pasadena, CA, USA.
E-mail address: j.razzellhollis@gmail.com (J. Razzell Hollis).

https://doi.org/10.1016/j.icarus.2022.115179
Received 24 May 2022; Received in revised form 25 June 2022; Accepted 6 July 2022
Available online 14 July 2022

chlorate. 3) A Raman peak at 1120 cm^{-1} in Dourbes could be sulfate or pyroxene, but elemental abundances from PIXL at that location are a better match to pyroxene. This study emphasizes the importance of analyzing co-located data from both instruments together, to obtain a more complete picture of sub-millimeter-scale mineralogy measured in situ in Jezero crater, Mars, by the *Perseverance* rover.

1. Introduction

In February 2021, the Mars 2020 *Perseverance* rover mission began investigating Jezero crater, located on the edge of Isidis Planitia, that hosted a lake and a river delta approximately 3.5 billion years ago [Schon et al., 2012; Goudge et al., 2015, 2017, 2018; Horgan et al., 2020; Mandon et al., 2020; Stack et al., 2020; Mangold et al., 2020, 2021; (Farley et al., 2022)]. An important mission goal is to characterize the geology of Mars, which will help us reconstruct its history, the evolution of its surface, and address whether the planet was potentially habitable in the past [Williford et al., 2018; Farley et al., 2020]. With these objectives in mind, the *Perseverance* rover was equipped with six scientific instruments capable of interrogating the surface of Jezero crater through imaging and chemical characterization, and detection of organic compounds. Two of those instruments – Scanning Habitable Environments with Raman and Luminescence for Organics and Chemicals (SHERLOC) and Planetary Instrument for X-ray Lithochemistry (PIXL) – are proximity science instruments designed to scan surfaces at small standoff distances with sub-millimeter-scale resolutions. PIXL and SHERLOC provide valuable in situ data on the spatial distributions and relationships of individual mineral phases that may be correlated to visible morphology, and were specifically chosen to complement each other's capabilities and maximize the scientific findings from rocks targeted for investigation and caching for a potential return to Earth. In order to provide geological context for the sample suite and inform future analyses performed on Earth, we must carefully characterize the elemental, molecular, and mineralogical composition of each target rock. Combining co-located data from these two instruments provides a novel and synergistic means of investigating rocks on the surface of Mars, beyond the capabilities of either instrument on its own.

Positioned at the end of the rover's robotic arm, PIXL and SHERLOC can approach natural and abraded rock targets within a few centimeters of the surface and can map their chemical and molecular constituents at spatial resolutions of ~100 μm. The PIXL instrument is a micro-X-Ray Fluorescence (XRF) spectrometer that provides spatially resolved elemental abundances (~120 μm resolution) and multispectral color images (~50 μm resolution) using its micro-context camera (MCC) [Allwood et al., 2020; Liu, 2022; Tice, 2022]. SHERLOC is a deep ultraviolet (DUV) Raman and fluorescence spectrometer that collects maps made of individual point spectra representative of molecular structure for both inorganic and organic compounds, with particular sensitivity to aromatic organics [Bhartia et al., 2021; Razzell Hollis et al., 2022]. SHERLOC operates alongside its own co-boresighted autofocus context imager (ACI), which provides high-resolution grayscale images at ~10.1 μm/pixel, and the Wide-Angle Topographic Sensor for Operations and eNgineering (WATSON), a focusable camera that provides 1648 × 1200-pixel high-resolution color images at working distances of ~1.8 cm to infinity with spatial resolutions in the 16–160 μm/pixel range. SHERLOC and PIXL are powerful analytical instruments on their own, but each specializes in the collection of certain types of data that interrogate specific compositional parameters and/or properties: SHERLOC can detect polyatomic ions in minerals such as sulfates and carbonates, but cannot always tell which cations are present, while PIXL can measure elemental abundances but cannot directly detect very low-mass elements such as H, C and O. Assessing multiple measurements from different kinds of analytical techniques on the same geologic sample allows for removal of ambiguity in drawing conclusions on local elemental, molecular, and mineralogical composition of the rocks. This, in turn, allows us to better interpret the geologic history of Jezero crater.

In this article, we use two abraded rock targets, Bellegarde and Dourbes, as case studies for the coordinated use of PIXL and SHERLOC instruments and data. Bellegarde is on the Rochette rock found in the Máaz formation of the crater floor, and Dourbes is on the Brac outcrop of the Bastide member in the Séítah formation of the crater floor (see Fig. 1a). Both targets have been analyzed with overlapping PIXL and SHERLOC scans (illustrated in Fig. 1b,c), providing data on both elemental and chemical composition. These data sets along with MCC, ACI, and WATSON images demonstrate the spatial distributions and relationships between different elements, minerals, chemical compounds, and textures. With these results in mind, future analyses that combine PIXL and SHERLOC data will allow for more robust interpretation of mineral assemblages. A complete understanding of the mineralogy of the units in Jezero crater, cross-cutting relationships, and alteration history of those rocks will be crucial as we attempt to constrain the formation and alteration mechanisms and, ultimately, the evolution and geologic history of Jezero crater and any aqueous processes that occurred in the lake.

2. Methods

2.1. PIXL operation

PIXL is a micro-X-ray fluorescence spectrometer (XRF) that collects elemental maps and operates alongside a micro-context camera (MCC), which collects a set of multispectral images in bands of ultraviolet (385 nm), blue (450 nm), green (530 nm) and near-infrared (735 nm; Allwood et al., 2020). Using range and topography measurements, obtained by the MCC, the multispectral dataset is radiometrically corrected to produce a composite near-infrared visible (NIRVIS) image and enable multispectral analysis, e.g. band ratio analysis, classification and modal analysis [Allwood et al., 2020; Liebe et al., in review]. PIXL scans sample surfaces with an X-ray beam using a range of scan types including grids, line scans, and high-resolution maps. The X-ray tube uses a rhodium anode, operating at 28 kV and 20 μA, and uses grazing-angle X-ray optics to focus the X-ray beam onto the surfaces to a minimum spot size of 120 μm. The focused X-ray beam hits the samples and induces X-ray fluorescence. The fluoresced X-rays are collected by two silicon drift detectors (SDD) with 160 eV resolution at 5.9 keV and count rates of ~8000 counts per second (cps) per detector. This allows PIXL to detect, map, and quantitatively assess the abundance of sodium (Na), magnesium (Mg), aluminum (Al), silicon (Si), phosphorous (P), chlorine (Cl), potassium (K), calcium (Ca), titanium (Ti), chromium (Cr), manganese (Mn), iron (Fe) as well as several trace elements. The optimal beam diameter is ~120 μm but varies slightly depending on the element, this is because of the differential excitation area and X-ray emission associated with lighter elements compared to those of heavier elements which results in a larger effective spot size for lighter elements. The analyses presented in this paper consist of high-resolution maps with 125 μm spacing between spots and measurement spot offsets equal to the nominal beam diameter for nearly continuous coverage of the targets' surfaces.

2.2. SHERLOC operation

SHERLOC is a deep ultraviolet Raman and fluorescence spectrometer that comes with a high-resolution imaging camera named WATSON. SHERLOC operates by scanning the target surface point-by-point in a grid using a 248.5794 nm pulsed laser, collecting Raman scattered and fluorescence photons emitted by illuminated material in the target's near subsurface [Bhartia et al., 2021]. The laser spot is annular in shape, ~110 μm in diameter at focus, and is fired in 40 μs pulses at 80 Hz, with

an estimated pulse energy of ~9 μJ at start of mission. Raman scattered and fluorescence photons are collected and measured simultaneously in a single spectrum between 250 and 354 nm, at a spectral resolution of 0.269 nm (~40 cm^{-1}) and 0.071 nm/pixel (~10 cm^{-1}/pixel) in the Raman region (250–275 nm). The detector is a 512 × 2048 pixel e2v 42–10 charge-coupled device (CCD) that is kept at −28 °C using a phase change material [Bhartia et al., 2021]. The laser spot is moved from point to point by an internal scanning mirror, and is capable of scanning up to 1296 points in an area as large as 7 × 7 mm. The instrument has an optical working distance of 48 mm and is focused using the co-boresighted autofocus context imager (ACI), which acquires a high-resolution, grayscale 14 × 16 mm image of the target surface at ~10.1 μm/pixel. SHERLOC's spectral calibration has an estimated uncertainty of ±5 cm^{-1} (±0.004 nm) in the 700–1800 cm^{-1} (253.0–260.2 nm) region, based on spectral analysis of calibration targets onboard the rover (Fries et al., 2022).

2.3. Target selection and data acquisition

Targets were selected by the science team and were chosen considering engineering requirements for the abrasion tool and scientific interest in particular targets. The abrasion tool requires a topography that does not exceed 20 mm roughness and an angle of 5° from the normal of the abrasion bit. Abrasion depth is defined by full depth of penetration through the entire abraded patch with 16 mm being the deepest depth. Therefore, some depth variation is possible across the patch.

The Bellegarde and Dourbes targets were both abraded to a depth of 7–10 mm to provide a relatively flat surface for characterization by PIXL and SHERLOC. *Perseverance*'s abrasion tool produces a circular abraded patch nominally 50 mm in diameter and 7–10 mm deep, which is then cleaned of dust/tailings using a jet of compressed gas from the gas Dust Removal Tool (gDRT) [Moeller et al., 2020]. *Perseverance*'s robotic arm places each instrument over a targeted spot on the abraded patch. The 3-sigma arm placement accuracy is 12 mm and targets are selected to ensure placement within the abraded patch area. Current experience on Mars indicates that the arm is reproducibly placed within 2 mm when a target has already been established and on the order of 3–4 mm on new targets.

2.3.1. Bellegarde

The Bellegarde target was abraded on sol 185 to a depth of 10 mm, then characterized by SHERLOC and PIXL on sol 186. SHERLOC

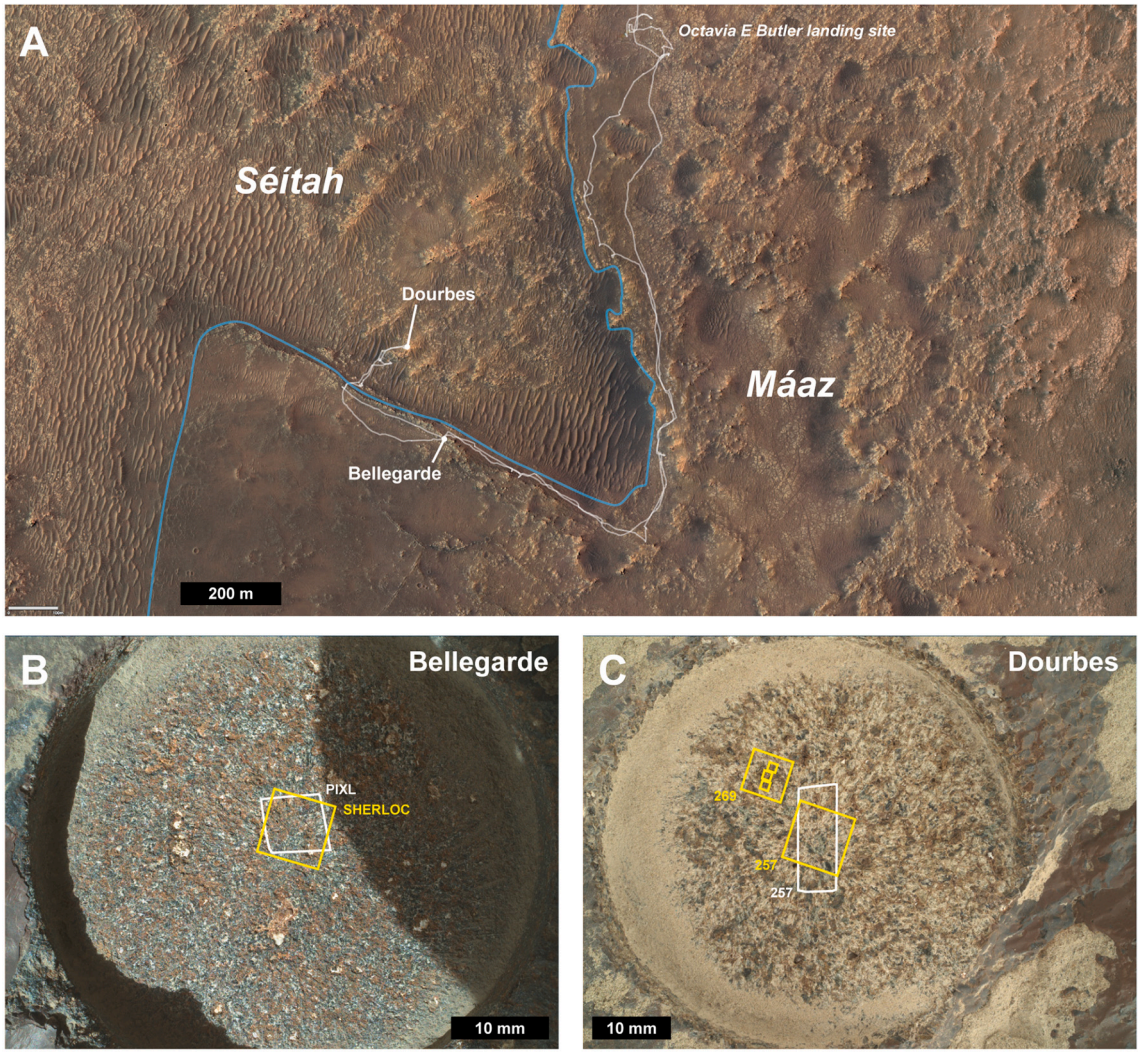

Fig. 1. a) HiRISE orbital image of the Jezero crater floor, focusing on the Mars 2020 *Perseverance* rover's Crater Floor Campaign path (marked in white). The locations of the Bellegarde and Dourbes abrasion targets are shown, while the line dividing Máaz and Séítah Formations is shown in blue. b) WATSON image of the Bellegarde abraded patch, illustrating the areas scanned by SHERLOC (yellow rectangles) and PIXL (white rectangle) on Sol 186. c) WATSON image of the Bellegarde abraded patch, taken at 7 cm standoff, illustrating the areas scanned by SHERLOC (yellow rectangles) and PIXL (white rectangle) on Sols 257 and 269. (For interpretation of the references to color in this figure legend, the reader is referred to the web version of this article.)

measurements consisted of one survey scan of 36 × 36 points in a 5 × 5 mm area at 15 pulses per point, and two high dynamic range (HDR) scans of 10 × 10 points in a co-located 7 × 7 mm area, both at 250 pulses per point. PIXL scanned a 6.5 × 6.5 mm area with 125 μm step spacing using a high-resolution map scan.

2.3.2. Dourbes

The Dourbes target was abraded on sol 253 to a depth of 7 mm, then characterized by SHERLOC and PIXL on sol 257. SHERLOC measurements consisted of one survey scan of 36 × 36 points in a 5 × 5 mm area at 15 pulses per point, and one HDR scan of 10 × 10 points in a co-located 7 × 7 mm area at 500 pulses per point. PIXL scanned a 4 × 12.5 mm region with a high-resolution map and 125 μm step spacing. Subsequent SHERLOC measurements on another part of Dourbes were conducted on sol 269 but are not included in this study due to lack of overlap with PIXL (see Fig. 1).

2.4. PIXL data processing

PIXL data are processed and visualized in PIXLISE, an XRF data processing software [Allwood et al., 2020]. The software uses PIQUANT [Allwood et al., 2020], a tool designed for the PIXL team to translate XRF spectra into element quantifications by relating peak intensities and widths to elemental abundance. These are co-registered to the multispectral observations from the MCC. PIXL also maps the distribution of elements, which can be visualized as elemental maps in PIXLISE. Diffraction signals can be identified in the data sets by comparing the spectra from each of the two detectors to identify any discrepancies. Such discrepancies highlight any peaks that result from X-ray diffraction rather than true presence of a given element.

For every map, element peaks are identified along with diffraction peaks and other instrument artifacts [Tanaka et al., 2017; Allwood et al., 2020; Tice, 2022]. Once all elements have been manually identified, PIQUANT fits observed spectra to theoretical fluorescence spectra generated from fundamental X-ray physics and measured properties of the PIXL instrument, accounting only for those elements that have been identified, and generates elemental abundances for the entire map area. The distribution of these elements and their abundances are then mapped across the scan area in PIXLISE. Regions of interest (ROI) can then be individually selected and the quantification process is repeated to generate quantitative elemental and oxide wt% abundances of these ROIs using bulk sum spectra. For areas of interest that are especially difficult to disentangle from the dominant minerals (e.g., carbonates, sulfates, and amorphous silicates), the elemental composition were calculated by subtracting out elements in the appropriate molar ratios for igneous minerals identified in the surrounding matrix by quantifications of specific regions that indicate silicate minerals like feldspar, olivine, pyroxene Fe-Ti-Cr oxides (Liu, 2022; Tice, 2022). The compositions of these ROIs are then assessed and visualized on ternary diagrams which show mixing relationships for complex mineral assemblages. This allows for the characterization of individual grains separately from bulk composition as well as the mix of mineral phases that comprise the rocks.

2.5. SHERLOC data processing

SHERLOC spectra are read out in three separate CCD regions, which are then recombined during processing to recreate the full 250–355 nm spectrum [Bhartia et al., 2021]. This is intended to optimize spectral resolution and minimize noise in the Raman region (250–275 nm). For each region in each spectrum, an active frame is acquired while the laser is firing and a dark frame for the same duration without laser illumination, which is then subtracted from the active frame to correct for dark current [Bhartia et al., 2021]. Initial data processing was done using NASA internal software, named Loupe. Full processing includes dark frame subtraction, normalization to measured laser output, and cosmic ray removal using the method described by Uckert et al. (2019). Further data processing was done using custom Python scripts, following methods developed by Razzell Hollis et al. (2021). This includes polynomial baseline subtraction, automatic peak detection, generating spectral intensity maps, and determining peak positions via Gaussian fitting. Spectral intensity maps were generated using three pre-defined spectral bands, and assigning the summed intensities of each band in each spectrum to the R, G, B values of the corresponding pixel, normalized to the 2% and 98% percentiles for all three bands across the entire map. Mineralogical assignments were done by comparing baselined SHERLOC spectra and fitted peak positions to the SHERLOC Spectral Library, a database of spectral standards for minerals and organic compounds measured on Earth using the Brassboard instrument, an optical analog of the SHERLOC flight model that was adapted to function under terrestrial ambient conditions. A detailed summary of the Spectral Library and the Brassboard instrument can be found in Razzell Hollis et al. (2021).

2.6. ACI/WATSON image processing

SHERLOC ACI images were flat-fielded using calibration images acquired on Sol 77. This procedure corrects for vignetting across the ACI field of view. Then, corresponding flat-fielded SHERLOC ACI and WATSON images for each target served as the base images for a secondary product that provides color and textural information that can be correlated to scan footprints. Image registration and processing was performed using a custom Python script that utilized corresponding ACI and WATSON (onboard focus merge) images for a target to create an overlay. Keypoints in each image were detected using the Binary Robust Invariant Scalable Keypoints (BRISK) method [Leutenegger et al., 2011], and subsequently matched with a Fast Library for Approximate Nearest Neighbors (FLANN) based matcher utilizing the OpenCV python package [Bradski, 2000]. If over 30 matches could be found between keypoints in each image, then hue, saturation, and values from the two images were blended to create a "colorized" ACI. This resulting product is most affected by the colors of the base WATSON image and its conditions of acquisition, such as mode of illumination (e.g., sunlight or LED). A similar process was used to colorize the PIXL MCC images.

3. Results and discussion

3.1. Spot sizes and implications for detection

PIXL and SHERLOC both operate by scanning the target surface point by point in a grid and measuring the response from any material in the illuminated area at each point. Differences in design and operating parameters mean that the two instruments illuminate (and thus interrogate) the surface differently, with implications for detection and specificity – particularly when dealing with very small features such as single mineral grains. The spot illuminated by PIXL is a circle approximately 120 μm in diameter at best focus (an illuminated area of ~11,000 μm^2), though for lighter elements the illuminated spot increases up to a diameter of ~230 μm (an area of ~41,500 μm^2) due the energy dependence of spot size for different elements (Tice et al., 2022). The spot illuminated by SHERLOC is a slightly elliptical annulus with an outer diameter of 110–115 μm and an inner diameter of 48–52 μm at best focus, with an illuminated area of ~8000 μm^2 [Bhartia et al., 2021]. Both spots are shown to scale in Fig. 2. If the two spots are centered perfectly on the same location, 100% of the SHERLOC spot overlaps with 19–72% of the PIXL spot, depending on elemental Z. Differences in scan grid parameters, imperfect placement accuracy and drift of the rover's robotic arm during operations mean that individual spots may not line up when the same target region is analyzed by PIXL and SHERLOC [Bhartia et al., 2021]. In terms of the areas of each target scanned, good overlap was achieved on both Bellegarde and Dourbes: on Bellegarde 73% of the SHERLOC HDR scan area overlaps with 91% of the PIXL scan

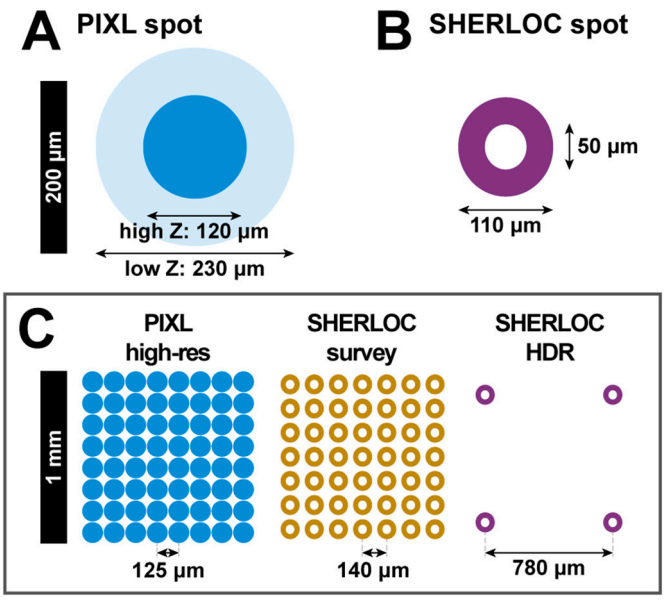

Fig. 2. Illustration of PIXL (a) and SHERLOC (b) illuminated spot sizes to scale, PIXL spot size increases with decreasing atomic number Z. c) The arrangement of measurement points for different PIXL and SHERLOC activities conducted at Bellegarde and Dourbes, shown for a 1 mm^2 area under ideal conditions.

area; on Dourbes 70% of the SHERLOC HDR scan area overlaps with 59% of the PIXL scan area (see Fig. 1b,c).

Fig. 2c illustrates how each instrument interrogates an area of 1 mm^2 using typical operating parameters. During a PIXL high-resolution scan, the measured points should be evenly spaced 125 µm apart, resulting in 64 points per square millimeter, though actual PIXL point positions may deviate from the idealized grid pattern due to surface topography, instrument angle, and thermal drift of instrument position (as seen in both the Bellegarde and Dourbes scans). A SHERLOC survey scan is done with a point to point spacing of ~140 µm, resulting in 49 points per square millimeter, while an HDR scan is done with a spacing of ~780 µm, resulting in only 4 points per square millimeter, but uses more laser pulses per point to produce a higher signal:noise (SNR) ratio for each measurement. Based on the estimated size of each spot and the spacing between points, PIXL will interrogate approximately 72–100% of the stated scan area depending on the element, while a SHERLOC survey and HDR will interrogate approximately 41% and 1.3% respectively (these do not include the inner circle of the SHERLOC spot, which receives comparatively little laser light due the annular shape of the beam).

These parameters are important for understanding how precise such co-located measurements can be when PIXL and SHERLOC interrogate a target surface. Both instruments illuminate relatively large areas in a single measurement, meaning that for surfaces with fine-scale (<100 µm grain size) heterogeneity, the resulting spectra will be an ensemble measurement of the various mineral phases interrogated, rather than single minerals. For PIXL, the larger effective spot size for lighter elements means that there will be more overlap between adjacent points, which may lead to mixing between adjacent minerals that are smaller than 100 µm and blurring of spatial features in the map. The presence of a particular mineral phase in a certain location also does not necessarily mean that both or either instruments will detect it, particularly if it is small, falls between measured points, or otherwise does not appreciably overlap with them. For SHERLOC, the annular shape of the laser spot means that there is a region in the center of the spot that is relatively unilluminated (and therefore provides little signal), such that a mineral grain <50 µm in size may be undetectable if the measurement point is directly centered on it. All of these factors interact when each instrument scans a target surface, and will influence whether or not a detectable signature is actually detected; non-detection of a particular mineral by either instrument does not necessarily equate to its absence in the target, as the mineral/element of interest may be either below the detection limit or be small enough to fall in the gap between illuminated points. This means that the absence of a mineral detection should not be interpreted as a definitive absence of that mineral, only that it was not seen by PIXL and SHERLOC. Still, PIXL and SHERLOC together provide a powerful ability to detect and interpret a range of minerals and phases on any given target at sub-millimeter resolution. This has allowed us to identify a range of igneous minerals and alteration phases in the rocks of the Jezero crater floor.

3.2. *Bellegarde/Máaz formation*

The majority of the Bellegarde target is composed of mafic minerals (mostly pyroxenes) and aluminosilicates (especially feldspars) whose textural relationships and composition suggest an igneous origin for the Máaz Formation (Farley et al., 2022). Additional iron-bearing mineral assemblages have also been identified that may be the result of serpentinization [Tosca et al., in prep.]. SHERLOC's sensitivity to iron-bearing minerals is limited due to low filter transmission at low Raman shifts (<800 cm^{-1}) and significant attenuation of the DUV laser by iron complexes, which limit the penetration of the DUV laser into the sample and reduce the measured Raman/fluorescence signal [Shkolyar et al., 2018; Carrier et al., 2019; Razzell Hollis et al., 2021]. As this study focuses on combined SHERLOC and PIXL detections, we will focus here on the low-iron secondary mineral assemblages that post-date the initial protolith formation/igneous mineralogy and may be the result of later aqueous activity (Farley, 2022; Scheller et al., 2022; Tice, 2022). The color WATSON image of the entire abraded Bellegarde patch is shown in Supplemental Fig. S1, along with the corresponding locations of SHERLOC and PIXL scans.

Bellegarde contains a suite of secondary minerals that are distinct from the majority iron-bearing igneous matrix and are distributed in discrete regions within the abraded patch. Many of these appear to fill former cracks, voids, or pore spaces and likely post-date emplacement of the igneous unit. These can be divided into three mineral phase categories: sulfates, chlorine-bearing minerals, and phosphate minerals, each described below.

3.2.1. *Sulfate minerals*

Sulfate regions stand out prominently in several distinct patches of Bellegarde, each approximately tens of µm up to 1 mm in size. Two of these in particular stand out. In WATSON, ACI, and MCC images, these regions are clearly visible as light toned to white patches that have sharp grain boundaries with the surrounding red-toned regions Fig. 3a), indicating that these are discrete minerals that are not intimately interwoven with the surrounding rock but instead likely fill a former void space. PIXL elemental maps show these as S-rich hotspots that are relatively depleted in Si and have sharp boundaries in elemental maps with the surrounding minerals (Fig. 3d,f). One sulfate patch, situated in the upper left-hand quadrant of the PIXL map, consists of two stacked crescent shapes of light-toned material (labeled ROI-1 in Fig. 3). This patch is readily distinguished by a strong Raman signal at 1013 ± 5 cm^{-1} that could be clearly observed in the survey map (Fig. 3b) and HDR map (Fig. 3c). The second sulfate patch is a small, oblong shape of light-toned, S-rich material situated in the bottom left-hand quadrant of the PIXL map (Fig. 3f), which coincides with a single sulfate spectrum detection in the SHERLOC HDR map (Fig. 3c), at a long exposure of 250 pulses per point.

The averaged SHERLOC sulfate spectrum for the double-crescent patch ROI-1 exhibits a major peak at 1013 ± 5 cm^{-1} and a minor peak at 1142 ± 5 cm^{-1}, while the single spectrum acquired from the lower left sulfate patch is weaker and exhibits a single peak at 1015 ± 5 cm^{-1} (Fig. 4a). A weak, broad hydration feature is also observed around 3350 cm^{-1} (see Supplemental Fig. S2). These spectra are similar to

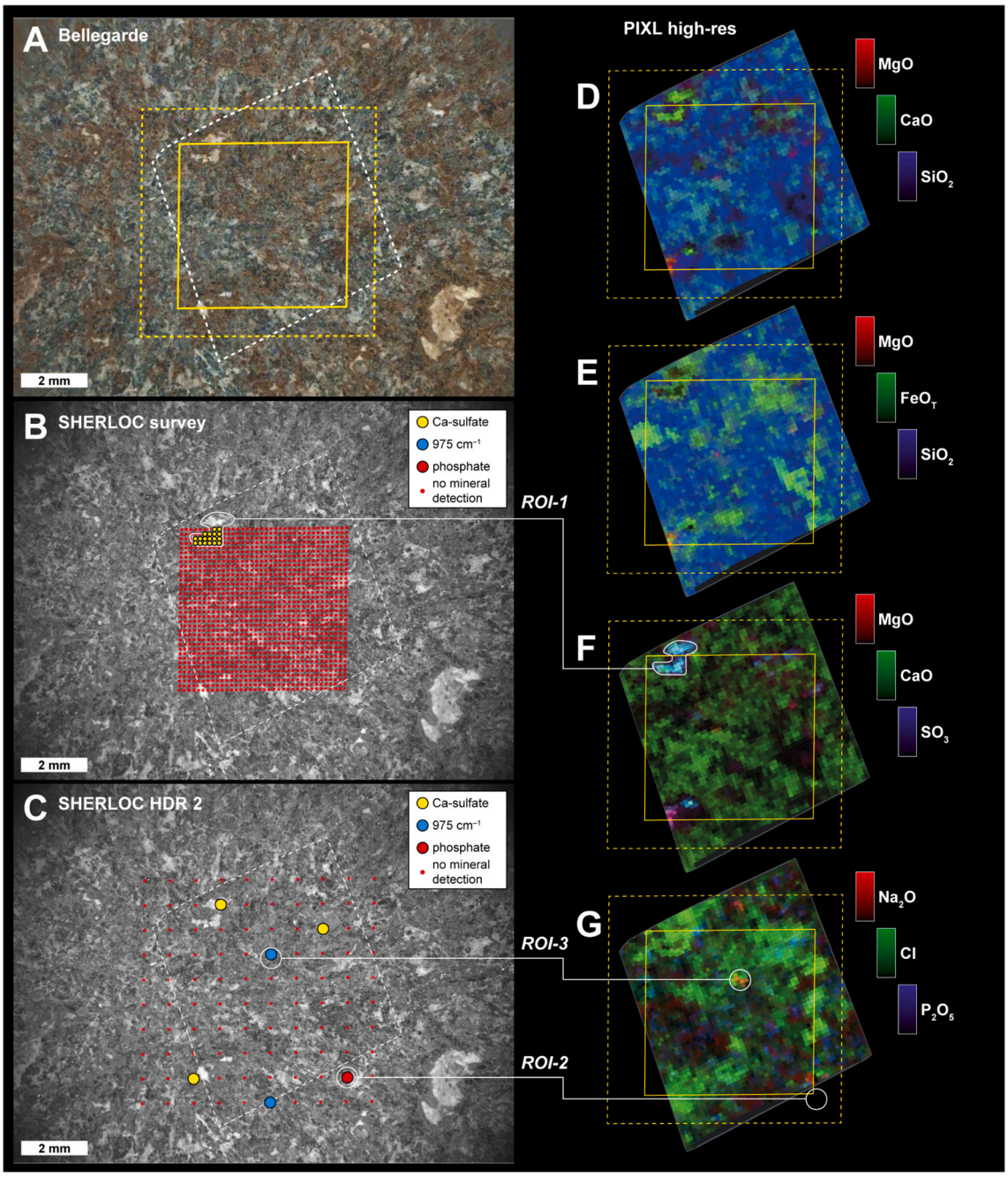

Fig. 3. (a) colorized SHERLOC ACI image, illustrating the footprints of the SHERLOC survey (yellow square) and HDR (yellow dashed square) maps, and the PIXL high-res map (white dashed square). SHERLOC measurement positions for the survey map (b) and HDR map (c) with spectral assignments to mineralogy. (d-g) PIXL elemental abundance maps indicating the spatial distribution of different key elements. Regions of Interest (ROIs) 1 to 3 are described with greater detail in Figs. 3–5 and Table 1.

reference spectra for terrestrial Ca-sulfate minerals analyzed with the SHERLOC laboratory analog instrument [Razzell Hollis et al., 2021]. Other sulfate minerals and salts were considered, but calcium sulfate dihydrate (gypsum) was the closest match for the measured Raman peak positions from both sulfate patches of Bellegarde (Fig. 4b). The low intensity of the hydrate peak relative to the major sulfate peak suggests that the sulfate in Bellegarde is only partially hydrated, similar to bassanite.

PIXL cation maps as well as quantifications from the S-bearing regions confirm that the centers of the double-crescent patch are Ca-rich, as is the center of the lower left sulfate patch. Elemental quantifications for these regions generated after stripping the surrounding sodium-chloride and iron-silicate minerals (supplemental data) show an approximate Mg:Ca molar ratio of 1:5.5 and overall oxide totals of ~84.3 wt% (Table 1). An Mg and Fe-rich rim surrounding the Ca-rich regions suggests a combination of Mg-sulfates and iron-bearing minerals surrounding the Ca-sulfate core. These minerals are likely a mixture of alteration products in the rims and in-fill of a possible void, though these were not detected by SHERLOC. The cation composition of the core of the sulfate region, however, confirms the interpretation by SHERLOC that it is a Ca-rich sulfate. It is important to note that neither H nor O can be detected by PIXL, meaning that the presence of these elements would result in low sums for the PIXL oxide quantifications. Therefore, a plausible explanation for the low overall oxide totals in the

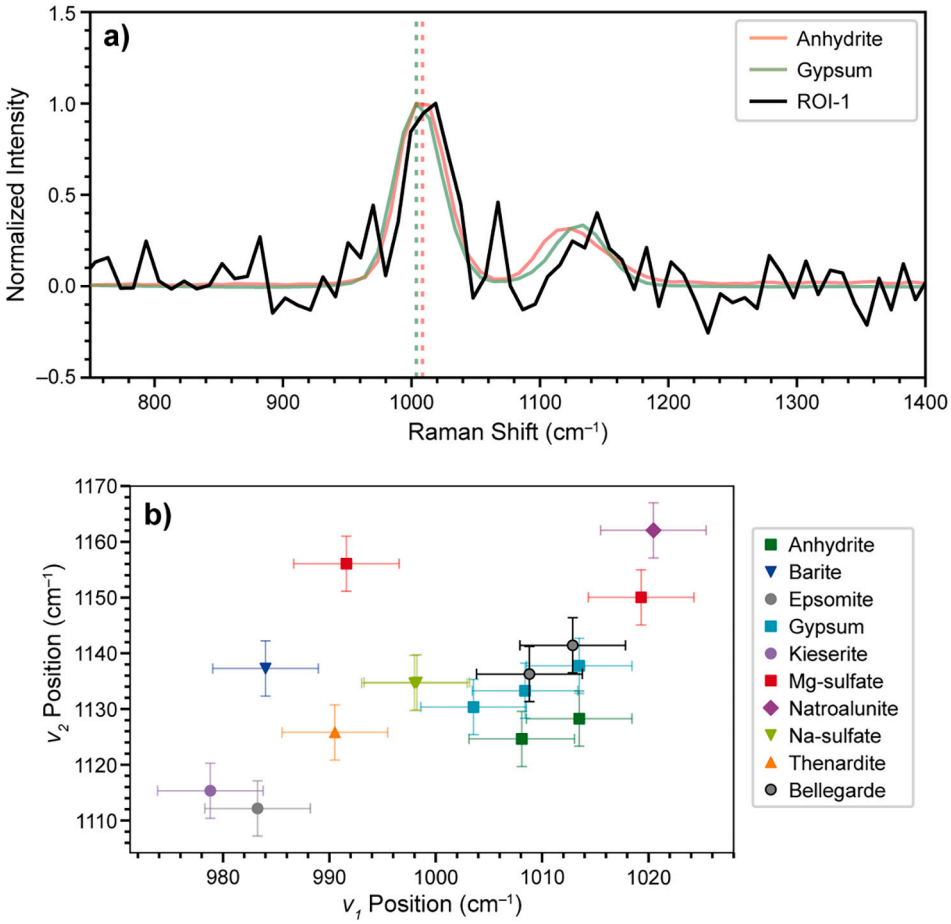

Fig. 4. a) SHERLOC Raman spectrum for the sulfate region ROI-1 in Bellegarde, showing the baselined average of 18 points from the survey map, normalized and compared to relevant reference spectra [Razzell Hollis et al., 2021]. b) The position of the major and minor peaks observed for the 2 sulfate patches in Bellegarde, plotted against reference positions for several different sulfate minerals and synthetic salts.

Table 1
PIXL quantifications for the core of the double-crescent sulfate patch, ROI-1, highlighted in Fig. 3.

Oxide	Oxide wt%
Na_2O	3.6 (±1.1)
MgO	2.8 (±0.5)
Al_2O_3	0.2 (±0.3)
SO_3	43.2 (±0.4)
CaO	21.6 (±1.1)
FeO	12.9 (±1.0)
Total	84.3

Quantifications were calculated after stripping of sodium-chloride salts and iron silicates that surround the crescent-shaped sulfate patch. Measurements include average error for the ROI measured (see supplemental document for PMC points and mineral stripping method).

Ca and S rich core is that the remaining weight percent of the Ca-sulfate minerals comes from water, though low totals may also be due, in part, to imperfect mineral stripping the mixture of minerals in this region. Hydration would also be consistent with the interpretation of the corresponding SHERLOC spectra that these Ca-sulfates are a low-hydration form such as bassanite. Thus, the combined data from the two instruments provide dual confirmation of the presence of highly localized hydrated Ca-sulfate that was deposited in the center of a fracture or void space after emplacement of the Bellegarde igneous unit.

3.2.2. *Phosphate minerals*

The most definitive phosphate detection occurs in a single SHERLOC measurement, on the edge of a light blue-gray patch in the bottom right-hand corner of the HDR scan (ROI-2 in Fig. 3). Because this detection occurs outside the area mapped by PIXL, the assignment cannot be confirmed by local elemental abundances; however, phosphorus was detected by PIXL throughout several gray-toned regions of Bellegarde (Fig. 3g). Overall, the area mapped by PIXL contains a 2.6 ± 0.4 wt% total P_2O_5 with P-rich areas containing ~10 wt% P_2O_5. These P-rich areas are typically gray-toned.

The SHERLOC spectrum from the point nearest ROI-2 exhibits a major Raman peak at 972 ± 5 cm^{-1} and a minor peak at 1049 ± 5 cm^{-1} (Fig. 5a). The major peak position is ambiguous, falling between reference values for the closest matching terrestrial phosphate (960 cm^{-1} for fluorapatite) and sulfate (979 cm^{-1} for kieserite) standards, but the position of the minor peak is more consistent with phosphate (~1050 cm^{-1}) than sulfate (~1140 cm^{-1}) (Fig. 5b). Perchlorate was also considered but the closest perchlorate reference (sodium perchlorate) is a poor match, with a major peak at 946 cm^{-1} and two minor peaks at 1088 and 1143 cm^{-1} (Scheller et al., 2022).

Despite the moderate total P content in Bellegarde, elemental maps rarely show large patches of single phosphate crystals or phosphate regions in the PIXL scan area. Instead, elemental maps show diffuse P throughout the scan area, especially in the red- and gray-toned regions. Unlike the sulfates, these appear to be small crystals scattered throughout the igneous matrix that are difficult to isolate from other minerals at PIXL's spatial resolution. The small size of the phosphate

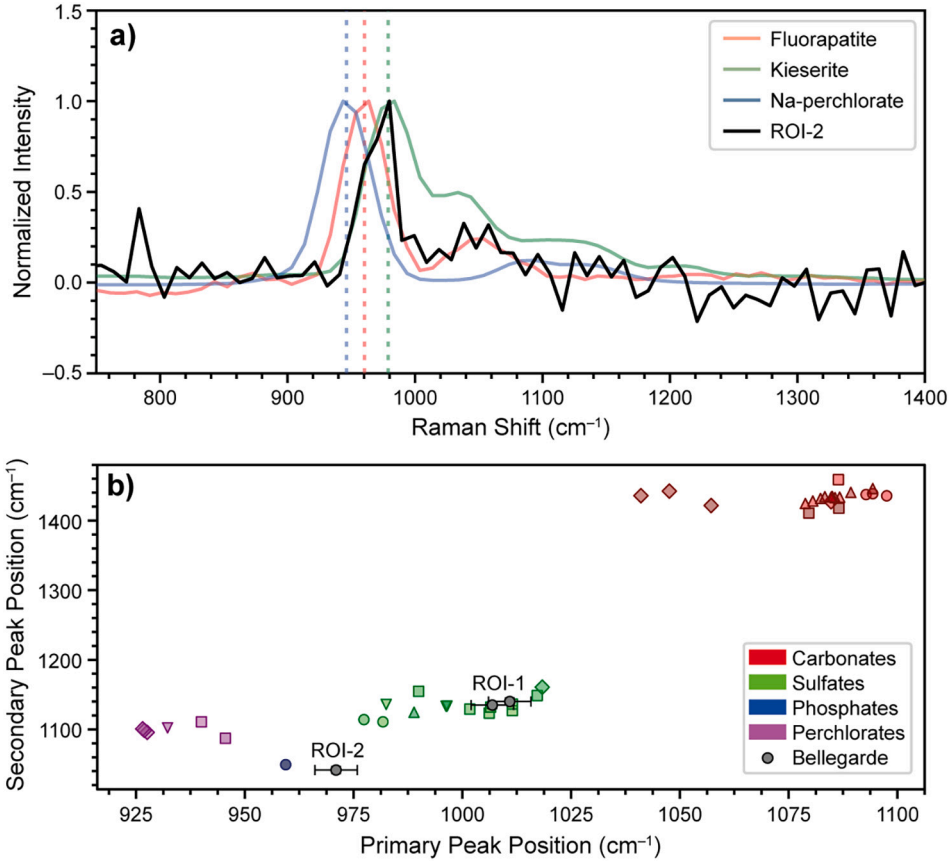

Fig. 5. a) SHERLOC Raman spectrum for the phosphate region ROI-2 in Bellegarde, normalized and compared to relevant reference spectra [Razzell Hollis et al., 2021; Scheller et al., 2022]. b) The position of the major and minor peaks, plotted against reference positions for several different minerals and synthetic salts containing perchlorate, phosphate, sulfate, and carbonate.

crystals and their distribution between other, larger minerals could explain why SHERLOC could not definitively detect any phosphate within the PIXL scan area, as small crystals are easy to miss and require longer exposures to provide detectable signal. It is possible that there are both microcrystalline phosphates scattered throughout the igneous matrix (similar phosphates have been seen in martian meteorites) and larger phosphate crystals that fill voids, similar to the sulfates in Bellegarde. However, because the PIXL and SHERLOC scan areas do not exactly overlap and each instrument did not scan the phosphates detected by the other, we cannot determine with certainty if there are multiple generations and types of phosphate. Still, even when direct co-location of data from both instruments is not possible, analysis of separate but texturally similar regions confirm the presence of phosphate minerals in Bellegarde and provide useful context for mineralogical assignments.

3.2.3. *Chlorine-bearing minerals*

Chlorine maps from PIXL show a similar distribution of chlorine-bearing minerals to that of phosphate minerals. Like the phosphates, Cl maps show that chlorine-bearing minerals occur as small domains diffusely scattered throughout the scan area. In some cases, these Cl-rich regions overlap with the diffuse distribution of Na. Like phosphate, the small size of these domains makes identification of individual phases difficult at the resolution of the PIXL map. Additional uncertainty in mineral identification also arises from the inability of PIXL elemental data to distinguish between halite and a sodium chlorate or sodium perchlorate, allof which have a 1:1 M ratio of Na and Cl and would thus be nearly identical based on PIXL data alone. Given a large enough crystal to provide a representative single measurement, elemental totals could indicate a presence of oxygen: if the totals are low, this would suggest chlorate or perchlorate, but if the totals are closer to 100%, this would suggest a chloride salt. Unfortunately, the chlorine-bearing minerals are too small to attempt this style of quantification in either Bellegarde or Dourbes.

Chloride salts are difficult to detect using SHERLOC as they lack Raman-active vibrational modes in SHERLOC's spectral range, 800–4000 cm^{-1} [Razzell Hollis et al., 2021], but SHERLOC is very sensitive to perchlorates, which typically exhibit a major Raman peak at 925–960 cm^{-1} and have been directly observed in other targets on Mars (Scheller et al., 2022). The closest SHERLOC HDR measurement is a single point <100 μm from the center of ROI-3, which exhibits a single, relatively weak peak at 979 ± 5 cm^{-1} (Fig. 6). This peak is apparent across multiple disparate points, varying between 970 ± 5 and 980 ± 5 cm^{-1} (Fig. 3c), but assignment of these spectra to a specific mineral phase is complicated by poor matching to reference spectra, low SNR and the lack of detectable minor peaks [Razzell Hollis et al., 2021]. We also note that the peak's FWHM of ~20 cm^{-1} is significantly smaller than that seen for definitive peaks of phosphate, sulfate, and other minerals (30–50 cm^{-1}) on both SHERLOC and the Brassboard instrument [Razzell Hollis et al., 2021; Uckert et al., 2021], which suggests that this may be a spectral artifact rather than a real Raman peak. If it is real, it is shifted by 30–40 cm^{-1} from the closest perchlorate reference (Fig. 6) and 20–30 cm^{-1} from the Martian Na-perchlorate detection previously reported by SHERLOC in Máaz Formation (Scheller et al., 2022). In the face of this evidence, we consider this peak to be inconsistent with perchlorate.

It is difficult to reconcile the amount of chlorine observed by PIXL with the lack of perchlorate signal measured by SHERLOC, unless the chlorine is present in the form of chloride salts. The Mars Science Laboratory (MSL) mission similarly encountered chlorine-containing phases

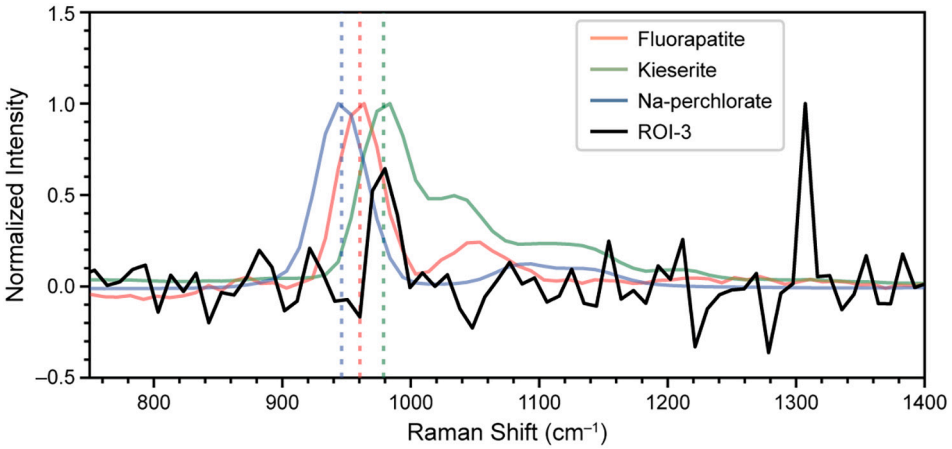

Fig. 6. SHERLOC Raman spectrum for the potential perchlorate/halite region ROI-3 in Bellegarde, normalized and compared to relevant reference spectra [Razzell Hollis et al., 2021].

at Gale crater, which were identified as perchlorate by the SAM instrument [Sutter et al., 2017] and halite by the CheMin and ChemCam instruments [Achilles, 2018; Thomas et al., 2019]. Both phases are likely present in Gale Crater and in Jezero Crater as well, and the perchlorate, if present, is low enough in abundance that it cannot be detected by either SHERLOC or CheMin. Further characterization of the Jezero samples once they have been returned to Earth by the Mars Sample Return mission will allow for a more accurate determination of the exact composition of these chlorine phases, and how they relate to the surrounding mineralogy of the Bellegarde target.

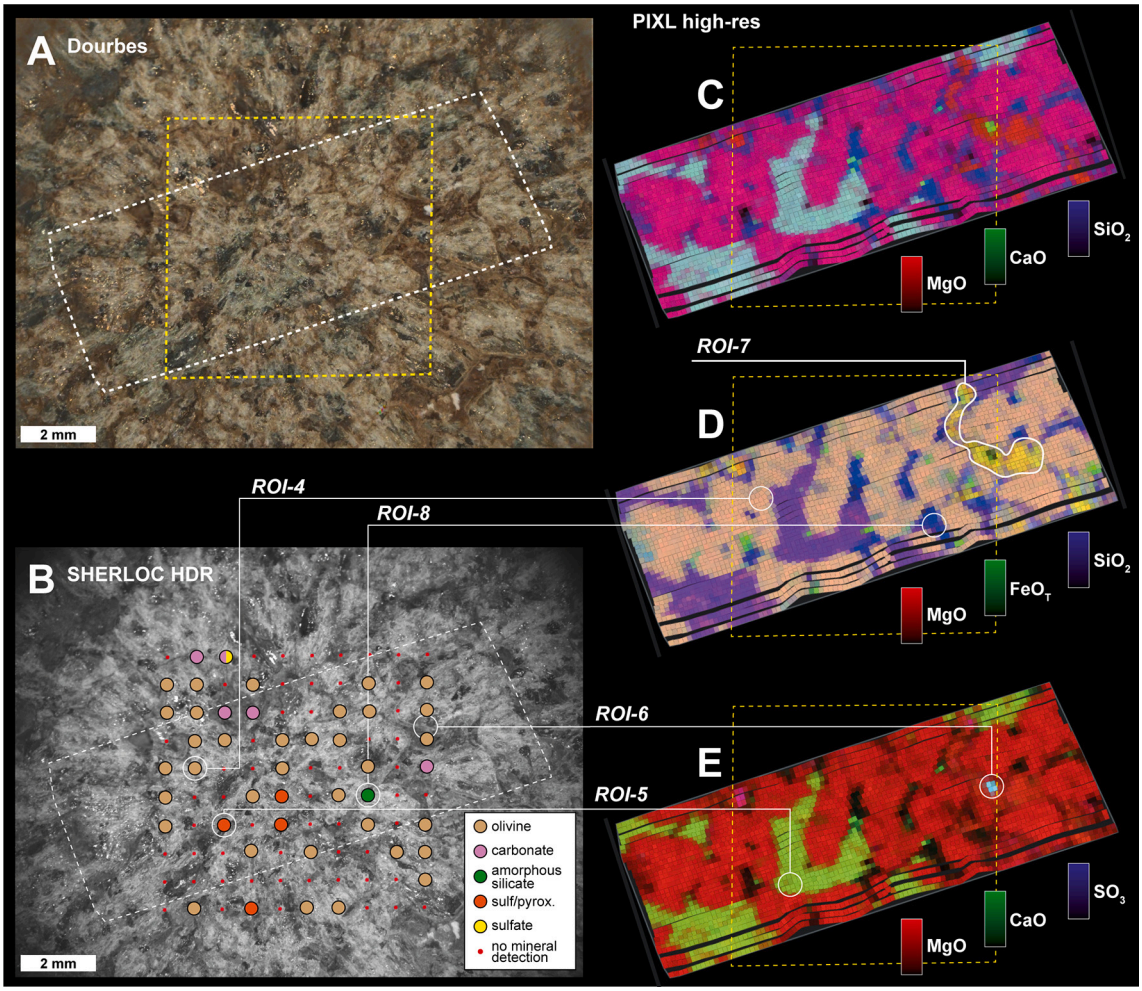

Fig. 7. (a) colorized SHERLOC ACI image, illustrating the footprints of the SHERLOC HDR map (yellow dashed square), and the PIXL high-res map (white dashed rectangle). (b) SHERLOC measurement positions for the HDR map, with spectral assignments to mineralogy. (c-e) PIXL elemental abundance maps indicating the spatial distribution of different key elements. Regions of Interest (ROIs) 4–8 are described with greater detail in Figs. 7–10 and Tables 2-4.

3.3. Dourbes/Séítah formation

Like Bellegarde, the protolith of Dourbes and the Séítah Formation are broadly interpreted as igneous and composed of mafic minerals and other silicates [Farley, 2022; Liu, 2022; Tice, 2022]. Specifically, the textures and mineral assemblages of this rock suggest that it is an olivine cumulate composed dominantly of olivines and clinopyroxenes. Unlike in Bellegarde, SHERLOC observes DUV Raman signal from secondary mineral assemblages, but also the primary olivine/pyroxene cumulate, permitting discussion of both (Fig. 7). In addition to the olivine and pyroxene, PIXL and SHERLOC detect sulfate as well as carbonate and amorphous silicate. The color WATSON image of the entire abraded Dourbes patch is shown in Supplemental Fig. S1, along with the corresponding locations of SHERLOC and PIXL scans.

3.3.1. Olivine

The most common texture in the PIXL elemental maps of Dourbes is an Mg-Fe olivine cumulate that closely resembles textures seen in igneous cumulate rocks on Earth and in meteorites of Martian origin (Liu et al., 2022). PIXL maps and quantifications of regions consistent with the mineral olivine show relatively high Mg and Fe (Fo_{55}; Table 2). PIXL maps also show that these olivine regions are rarely homogeneous; they appear patchy with heterogeneously distributed spots that are either Fe-Mg enriched or Si enriched relative to the bulk composition (Fig. 7; Supplemental Figs. 2 and 3). WATSON and ACI images show these as a mixture of tan and green-gray toned regions, with a mixture of tan, green, and red tones visible in MCC color stacks. This has been interpreted to be the result of later aqueous alteration of the olivine that resulted in some dissolution of the olivine and re-precipitation of silica-rich or Fe-Mg rich minerals (Tice et al., 2022). One such region is ROI-4 in Fig. 7.

These olivine regions are also apparent in the SHERLOC HDR map, detectable by a single Raman peak at 830 to 840 cm^{-1}. The average spectrum for all points assigned to olivine is shown in Fig. 8, to provide the best possible SNR, and has an averaged position of 831 ± 5 cm^{-1}. The spectrum exhibits a single Raman peak rather than the olivine doublet at 820 and 850 cm^{-1} usually reported under other excitation wavelengths, because the doublet is convoluted by SHERLOC's spectral resolution of ~40 cm^{-1} [Breitenfeld et al., 2018; Bhartia et al., 2021; Scheller et al., 2022]. Similar convolution is also evident in reference spectra for olivines acquired using the SHERLOC Brassboard instrument, which has a spectral resolution of ~50 cm^{-1} [Razzell Hollis et al., 2021]. The convoluted peak position is shifted to lower wavenumbers compared to available reference spectra, which were obtained exclusively from Mg-rich olivines between Fo# 80 and 90 [Razzell Hollis et al., 2021], and indicates that the olivines in Dourbes are richer in iron than these standards [Kuebler et al., 2006; Scheller et al., 2022]. This is consistent with PIXL measurements of the Mg:Fe ratio for the olivine cumulate.

Table 2
PIXL quantifications of major elements in olivine in Dourbes. Measurements include average error for the ROI measured (see supplemental document for PMC points).

Oxide	Oxide wt%
Na_2O	0.4 (±0.8)
MgO	24.8 (±1.4)
Al_2O_3	0.2 (±0.2)
SiO_2	35.9 (±1.8)
Cl	0.2 (±0.1)
CaO	0.4 (±0.2)
MnO	0.6 (±0.2)
FeO-T	36.5 (±1.8)
Total	99

3.3.2. Sulfate and pyroxene

The other dominant mineral that creates the olivine cumulate texture in Dourbes is pyroxene (Liu et al., 2022), evidenced by PIXL maps and quantifications. These pyroxenes are augites, Ca-Mg-Fe rich pyroxenes (Table 3; Supplemental Fig. 2) that engulf and surround the olivines in the PIXL maps (Fig. 7c,d; Supplemental Fig. 2), with one particularly large pyroxene region ROI-5 in Fig. 7. In WATSON and colorized ACI images, these regions appear green-gray toned with small dark spots scattered throughout. MCC color stacks show these regions as mottled green to dark gray toned regions.

SHERLOC also detects a number of spectra in the area of ROI-5 that exhibit a possible pyroxene peak around 1000 ± 5 cm^{-1}; the average of these spectra is shown in Fig. 9. This peak is difficult to assign confidently to any one particular mineral: it is significantly shifted compared to the reference peak of diopside, which occurs at 1016 cm^{-1}, it is a closer match to augite, which has a broad, low signal peak around ~1007 cm^{-1}, but is also very similar to the major peak exhibited by hydrated Na-sulfates like thenardite, around 990–1005 cm^{-1} [Shkolyar and Farmer, 2018; Razzell Hollis et al., 2021]. However, corresponding PIXL data do not show either Na or S in this region, and local elemental abundances are rich in Si, Mg, and Al. These elements and their relative abundances are more consistent with pyroxene than Na-sulfate. Thus, the combined PIXL measurements of local elemental composition and SHERLOC spectra together support assignment to a specific pyroxene mineral.

There are two unambiguous single-instrument sulfate detections in Dourbes, but comparative analysis of these minerals using both instruments is precluded by measurement positions. SHERLOC detected a single point with overlapping sulfate and carbonate peaks in the top left corner of the SHERLOC HDR map (Fig. 7b), but this falls outside the PIXL scan area. PIXL also detected a single sulfate region at the right side of its scan area, appearing as a bright 4-pixel S region (ROI-6 in Fig. 7). This spot also contains Ca and Mg, indicating that it is a mixture of Ca- and Mg-sulfates, similar to the sulfate regions detected in Bellegarde. While this region is technically within the SHERLOC HDR scan area, it is very small (~200 μm wide) and falls in the ~670 μm gap between the nearest two SHERLOC point measurements, meaning that there is no SHERLOC spectrum of that location. However, given the similarity of the mineral composition to that of the sulfate in Bellegarde, it can confidently be assigned as a Ca-sulfate by PIXL alone. These mineral detections highlight the limitations of co-located measurements. Even overlapping scan areas can still result in partial data return – especially when dealing with very small mineral regions that may be missed by one scan or the other. Obtaining a more precise co-location of individual points is currently beyond the targeting capabilities of the arm-mounted instruments, as dictated by arm placement accuracy and drift [Allwood et al., 2020; Bhartia et al., 2021].

3.3.3. Carbonate

SHERLOC detected carbonate minerals in multiple spots across the Dourbes scan area, usually associated with darker, brown-toned regions of the surface (Fig. 7b). These detections occur in two distinct areas, the upper left corner and right side of the HDR map, and are indicated by a relatively narrow peak at 1080 ± 5 cm^{-1} that corresponds to the major peak of carbonate, as shown in Fig. 10 [Razzell Hollis et al., 2021]. The position and width of the peak is consistent with Ca-carbonate, but there are a number of carbonates that are within the ±5 cm^{-1} uncertainty of the observed peak position. The assignment could not be corroborated by minor peak positions, as the expected carbonate peaks at ~1440 and ~1750 cm^{-1} are not detected.

PIXL is not capable of directly detecting carbonate because X-rays emitted from lighter elements like C and O are not seen by PIXL's detectors. It can, however, detect regions that likely contain an abundance of carbonate based on low element totals that result from the presence of unaccounted-for C and O. One region demonstrates this capability: a narrow, sinuous area of dark brown material that fills the gap between

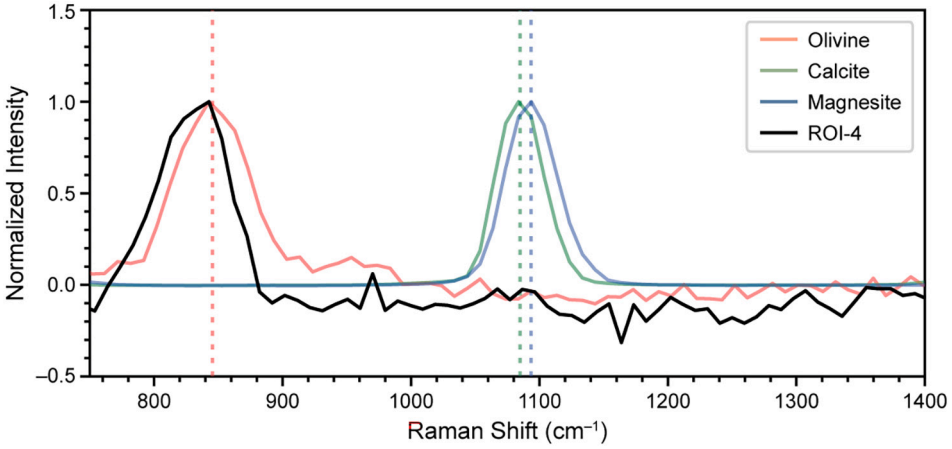

Fig. 8. Average SHERLOC Raman spectrum for the olivine region ROI-4 in Dourbes, normalized and compared to relevant reference spectra [Razzell Hollis et al., 2021].

Table 3
PIXL quantifications of pyroxene in Dourbes. Measurements include average error for the ROI measured (see supplemental document for PMC points).

Oxide	Oxide wt%
Na_2O	0.8 (±0.7)
MgO	14.2 (±0.8)
Al_2O_3	1.0 (±0.3)
SiO_2	50.6 (±2.5)
Cl	0.1 (±0.1)
CaO	17.6 (±0.9)
TiO_2	0.3 (±0.2)
Cr_2O_3	0.3 (±0.2)
MnO	0.4 (±0.2)
FeO-T	12.1 (±0.6)
Total	97.4

olivines in the upper right corner of the PIXL scan area (ROI-7 in Fig. 7) is rich in Mg and Fe and low in Si (Fig. 7d; Table 4; Supplemental Figs. S3-S4). These carbonates were quantified after mineral stripping analyses (see supplemental data) to remove elemental contribution from feldspars, pyroxenes, and sulfates, all of which directly contact the carbonate region and result in mixing of mineral phases at the resolution of the PIXL scans. When quantified as oxide weight percentages, this region shows abundant Fe and Mg, but with element totals of ~59.1 wt %. This is approximately what we would expect for carbonate, with the remaining 41 wt% accounted for by CO_3. Indeed, when this region is instead quantified as a carbonate in PIXLISE, the element totals are much closer to 100%. Thus, this area likely represents an Mg-Fe carbonate. Interestingly, the Mg/Fe ratio of this region is similar to that of the Mg/Fe mol ratio of the olivine. If this carbonate formed through dissolution of olivine, it likely formed under low water:rock ratios in which the carbonate precipitated rapidly from solution with approximately equivalent Fe and Mg activities. This would result in the precipitation of carbonate with the same Fe/Mg composition as that of the olivine from which the cations were released (Tice et al., 2022). PIXL data additionally show that this area has less diffraction than olivine and pyroxene regions, indicating that it is either x-ray amorphous or poorly crystalline with crystal sizes smaller than the resolution of the PIXL map (Tice et al., 2022). Unfortunately, the SHERLOC carbonate detections in Dourbes are infrequent enough to make correlation to PIXL cation data difficult. However, based on the similar texture and color, and the presence of a SHERLOC carbonate detection in the same area, this may be sufficient to correlate SHERLOC and PIXL data on carbonate-bearing mineralogy in Dourbes.

The detection of Mg and Fe (and low Ca) in the ROI-7 region is reconcilable with SHERLOC's observations of a carbonate peak at 1080 cm^{-1}, which we had tentatively assigned to Ca-carbonate rather than Mg-Fe-rich carbonate. Assignment was based on available reference spectra in the DUV spectral library, which were collected using the

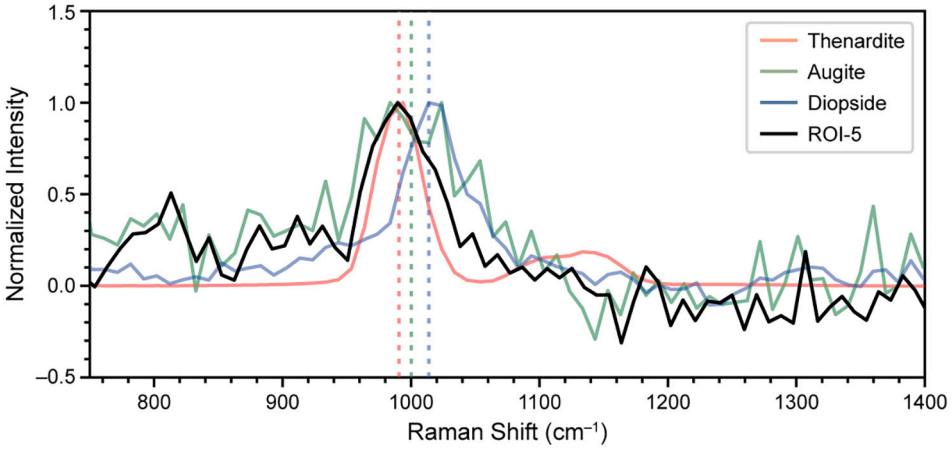

Fig. 9. Average SHERLOC Raman spectrum for the potential sulfate/pyroxene region ROI-5 in Dourbes, normalized and compared to relevant reference spectra [Razzell Hollis et al., 2021].

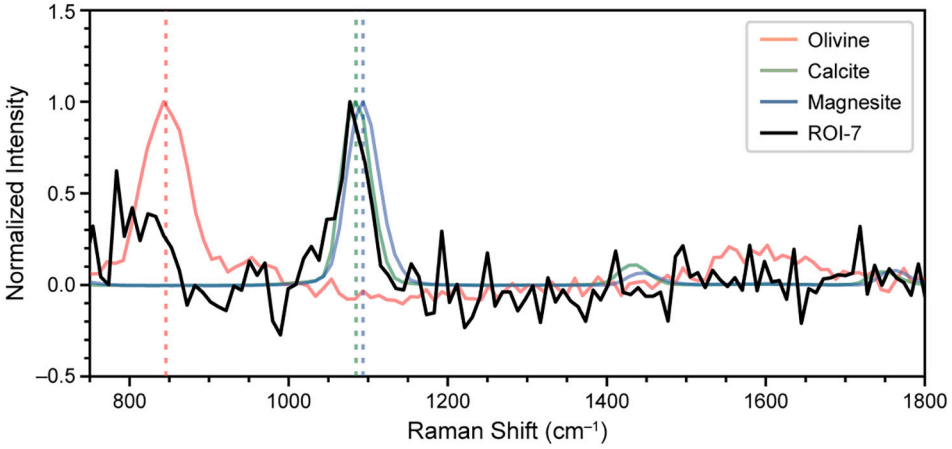

Fig. 10. Average SHERLOC Raman spectrum for the carbonate region ROI-7 in Dourbes, normalized and compared to relevant reference spectra [Razzell Hollis et al., 2021].

Table 4
PIXL quantification of potential Mg-Fe carbonate.

Oxide	Oxide wt%
Na_2O	0.3 (±1.0)
MgO	19.4 (±1.3)
MnO	1.1 (±0.3)
FeO-T	38.3 (±2.1)
Total	59.1

Quantifications were calculated after stripping elemental contribution from the surrounding feldspar, pyroxene, and sodium chloride phases. Measurements include average error for the ROI measured (see supplemental document for PMC points and mineral stripping method).

SHERLOC Brassboard analog instrument. This library includes siderite but no other Fe-bearing carbonates, and siderite did not produce enough signal to provide a measurable peak position for comparison, though we note that the Brassboard analog is less sensitive than SHERLOC itself [Razzell Hollis et al., 2021]. However, literature values for siderite put its major Raman peak at the same position as that of calcite, ~1086 cm^{-1}, and almost within uncertainty of the observed peak position [Rull et al., 2004]. Therefore, the best concatenation of SHERLOC and PIXL data is that we are observing an Mg-Fe carbonate rather than a Ca-carbonate, and that it tends to occur in the dark, brown-toned regions between olivines. This, combined with the similar relative proportions of Mg and Fe in the olivine and carbonate, supports interpretations of Martian carbonates as products of aqueous alteration of Mg-Fe olivine (Scheller et al., 2022; Tice, 2022).

3.3.4. *Amorphous silicate*

Several small regions between the olivine grains throughout the PIXL scan region stand out as being distinct from the previously identified silicate minerals that comprise the bulk of the rock because they show significantly higher wt% SiO_2 than the igneous minerals. These regions contain some Fe and Mg, but less than would be expected in olivine, very little Ca compared to what would be expected in pyroxene, and little Na or Al compared to what would be expected in feldspar, all of which are also present in the scan area (Fig. 7; Supplemental Figs. 2 and 3). Like the chlorine-bearing phases and phosphates, these silica-rich regions are small (Fig. 7d, particularly the region ROI-8; Supplemental Figs. 2 and 3) making characterization of single crystals difficult at the resolution of a PIXL scan. However, PIXL data do reveal a lack of diffraction in some of these regions, similarly to the carbonates, indicating that the material is likely x-ray amorphous or poorly crystalline (Tice et al., 2022).

Detection of low Fe-Mg silicates by PIXL is confirmed by at least one SHERLOC measurement in the same region of Dourbes, which exhibits a single broad Raman peak centered at 1070 ± 5 cm^{-1} (shown in Fig. 11). This broad, relatively weak peak is consistent with amorphous silicate

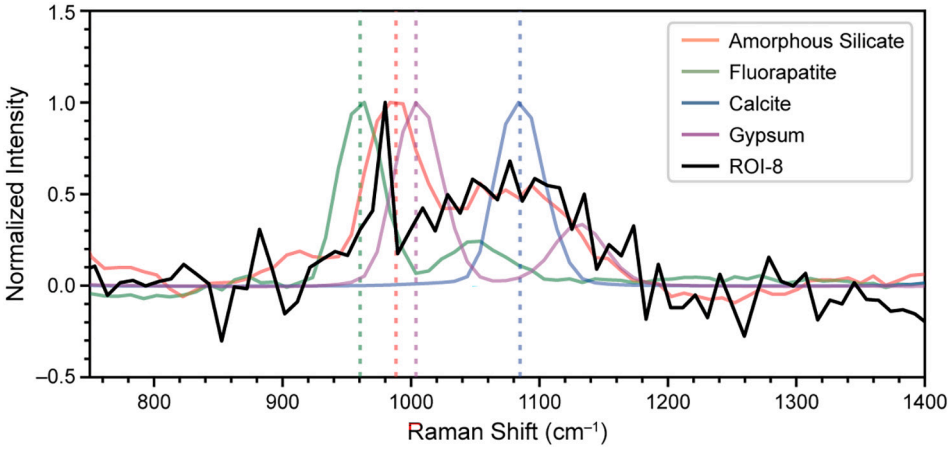

Fig. 11. SHERLOC Raman spectrum for the amorphous silicate region ROI-8 in Dourbes, normalized and compared to relevant reference spectra [Razzell Hollis et al., 2021; Moore et al., submitted].

rather than a crystalline silica such as quartz [Mysen et al., 1982; Bellot-Gurlet et al., 2004; Fu et al., 2017]. The sharp peak that appears in the SHERLOC spectrum at 976 ± 5 cm^{-1} is <2 pixels wide (<20 cm^{-1}) and as such is considered a spectral artifact (e.g., a cosmic ray) rather than a real Raman peak, even though it appears to coincide with the surface Si–OH stretching mode seen at 988 cm^{-1} in the amorphous silicate reference spectrum. We also considered possibility of quartz contributing to PIXL's observed silica signal, but the major Raman peak of quartz (at 476 cm^{-1}) and its triplet of minor peaks (at 1084, 1165, and 1232 cm^{-1}) are not detected in the ROI-8 region or any other silica-rich area [Razzell Hollis et al., 2021]. This appears to indicate that the low Fe-Mg silicate observed by PIXL is amorphous rather than crystalline. Based on their distribution around and between olivine grains as well as their presence alongside Mg/Fe carbonates, these silicates have been interpreted as the result of aqueous alteration of the olivine, resulting in dissolution and reprecipitation of amorphous Mg/Fe silicates and Mg/Fe carbonates (Tice et al., 2022).

4. Conclusions

The Mars 2020 *Perseverance* Rover payload was designed with the specific aim of combining data types to gain a more holistic understanding of the chemistry, mineralogy, composition, organic preservation, and textures of the rocks in Jezero crater. This is especially true of the two proximity science instruments on the robotic arm, PIXL and SHERLOC, which were selected for their ability to conduct micro-scale mapping of elemental and molecular data, which can then be combined to provide more complete geological interpretations than is possible with either instrument alone. The data presented here reinforce the rationale behind the payload selections for proximity science and provide a foundation for future paired micro-analyses on Mars. Using combined PIXL and SHERLOC datasets, we confidently identified 6 mineral phases (sulfate, halite, phosphate, olivine, pyroxene, carbonate) in the Bellegarde and Dourbes targets, located in Máaz and Séítah formations respectively, and began to characterize two additional phases (perchlorate and amorphous silicate) either present in trace amounts or diffusely distributed throughout the targets. With these mineral identifications, the Mars 2020 science team has been able to make significant strides in interpreting the protolith lithology of these rocks and the subsequent aqueous alteration [cite other papers]. Thus, these instruments, when combined, provide a powerful method for interpreting the mineralogy and chemical composition of rocks in Jezero crater. Paired, co-located analyses should be considered a critical part of proximity target investigation by *Perseverance* going forward.

Declaration of Competing Interest

None.

Acknowledgements

The work described in this paper was partially carried out at the Jet Propulsion Laboratory, California Institute of Technology, under a contract with the National Aeronautics and Space Administration. PIXLISE software was designed by teams from the Queensland University of Technology (QUT) and the NASA/Caltech/Jet Propulsion Laboratory through the Data to Discovery incubation program for science analysis tools as part of JPL's Data Science Program. Loupe was developed at the Jet Propulsion Laboratory by K. Uckert. J.R.H. was supported by a NASA Postdoctoral Program fellowship administered by the Universities Space Research Association on behalf of NASA. J.R.H., S.S., and others were also supported by the 107415 Mars 2020 Phase-E grant. K.R.M was supported by a NASA R&TD grant as well as the PIXL instrument team and the Simons Foundation. S.S. acknowledges support from NASA under award number 80GSFC21M0002. Data availability: The data used for the study is to be released on the Planetary Data System (PDS).

Appendix A. Supplementary data

Supplementary data to this article can be found online at https://doi.org/10.1016/j.icarus.2022.115179.

References

Achilles, C.N., 2018. Analyses of Crystalline and X-Ray Amorphous Materials in Gale Crater Rocks and Soils. Doctoral dissertation. University of Arizona Open Repository.

Allwood, A.C., Wade, L.A., Foote, M.C., Elam, W.T., Hurowitz, J.A., Battel, S., Dawson, D. E., Denise, R.W., Ek, E.M., Gilbert, M.S., King, M.E., Liebe, C.C., Parker, T., Pedersen, D.A.K., Randall, D.P., Sharrow, R.F., Sondheim, M.E., Allen, G., Arnett, K., Au, M.H., Basset, C., Benn, M., Bousman, J.C., Braun, D., Calvet, R.J., Clark, B., Cinquini, L., Conaby, S., Conley, H.A., Davidoff, S., Delaney, J., Denver, T., Diaz, E., Doran, G.B., Ervin, J., Evans, M., Flannery, D.O., Gao, N., Gross, J., Grotzinger, J., Hannah, B., Harris, J.T., Harris, C.M., He, Y., Heirwegh, C.M., Hernandez, C., Hertzberg, E., Hodyss, R.P., Holden, J.R., Hummel, C., Jadusingh, M.A., Jørgensen, J.L., Kawamura, J.H., Kitiyakara, A., Kozaczek, K., Lambert, J.L., Lawson, P.R., Liu, Y., Luchik, T.S., Macneal, K.M., Madsen, S.N., McLennan, S.M., McNally, P., Meras, P.L., Muller, R.E., Napoli, J., Naylor, B.J., Nemere, P., Ponomarev, I., Perez, R.M., Pootrakul, N., Romero, R.A., Rosas, R., Sachs, J., Schaefer, R.T., Schein, M.E., Setterfield, T.P., Singh, V., Song, E., Soria, M.M., Stek, P.C., Tallarida, N.R., Thompson, D.R., Tice, M.M., Timmermann, L., Torossian, V., Treiman, A., Tsai, S., Uckert, K., Villalvazo, J., Wang, M., Wilson, D. W., Worel, S.C., Zamani, P., Zappe, M., Zhong, F., Zimmerman, R., 2020. PIXL: planetary instrument for X-ray lithochemistry. Space Sci. Rev. 216, 134.

Bellot-Gurlet, L., Bourdonnec, F.-X.L., Poupeau, G., Dubernet, S., 2004. Raman micro-spectroscopy of western Mediterranean obsidian glass: one step towards provenance studies? J. Raman Spectrosc. 35, 671–677.

Bhartia, R., Beegle, L.W., DeFlores, L., Abbey, W., Razzell Hollis, J., Uckert, K., Monacelli, B., Edgett, K.E., Kennedy, M.R., Sylvia, M., Aldrich, D., Anderson, M., Asher, S.A., Bailey, Z., Boyd, K., Burton, A.S., Caffrey, M., Calaway, M.J., Calvet, R., Cameron, B., Caplinger, M.A., Carrier, B.L., Chen, N., Chen, A., Clark, M.J., Clegg, S., Conrad, P.G., Cooper, M., Davis, K.N., Ehlmann, B.L., Facto, L., Fries, M.D., Garrison, D.H., Gasway, D., Ghaemi, F.T., Graff, T.G., Hand, K.P., Harris, C., Hein, J. D., Heinz, N., Herzog, H., Hochberg, E., Houck, A., Hug, W.F., Jensen, E.H., Kah, L. C., Kennedy, J., Krylo, R., Lam, J., Lindeman, M., McGlown, J., Michel, J., Miller, E., Mills, Z., Minitti, M.E., Mok, F., Moore, J., Nealson, K.H., Nelson, A., Newell, R., Nixon, B.E., Nordman, D.A., Nuding, D., Orellana, S., Pauken, M., Peterson, G., Pollock, R., Quinn, H., Quinto, C., Ravine, M.A., Reid, R.D., Riendeau, J., Ross, A.J., Sackos, J., Schaffner, J.A., Schwochert, M., Shelton, M.O., Simon, R., Smith, C.L., Sobron, P., Steadman, K., Steele, A., Thiessen, D., Tran, V.D., Tsai, T., Tuite, M., Tung, E., Wehbe, R., Weinberg, R., Weiner, R.H., Wiens, R.C., Williford, K., Wollonciej, C., Wu, Y.-H., Yingst, R.A., Zan, J., 2021. Perseverance's scanning habitable environments with Raman and luminescence for organics and chemicals (SHERLOC) investigation. Space Sci. Rev. 217, 58. https://doi.org/10.1007/s11214-021-00812-z.

Bradski, G., 2000. The OpenCV library. J. Softw. Tools. 2000.

Breitenfeld, L.B., Dyar, M.D., Carey, C.J., Tague, T.J., Wang, P., Mullen, T., Parente, M., 2018. Predicting olivine composition using Raman spectroscopy through band shift and multivariate analyses. Am. Mineral. 103 (April), 1827–1836.

Carrier, B.L., Abbey, W.J., Beegle, L.W., Bhartia, R., Liu, Y., 2019. Attenuation of ultraviolet radiation in rocks and minerals: implications for Mars science. J. Geophys. Res. Planets 124 (10), 2599–2612. https://doi.org/10.1029/2018JE005758.

Farley, K.A., Williford, K.H., Stack, K.M., Bhartia, R., Chen, A., de la Torre, M., Hand, K., Goreva, Y., Herd, C.D.K., Hueso, R., Liu, Y., Maki, J.N., Martinez, G., Moeller, R.C., Nelessen, A., Newman, C.E., Nunes, D., Ponce, A., Spanovich, N., Willis, P.A., Beegle, L.W., Bell, J.F., Brown, A.J., Hamran, S.-E., Hurowitz, J.A., Maurice, S., Paige, D.A., Rodriguez-Manfredi, J.A., Schulte, M., Wiens, R.C., 2020. Mars 2020 Mission overview. Space Sci. Rev. 216, 142.

Farley, K., et al., 2022. Aqueously-altered igneous and sedimentary rocks on the floor of Jezero crater, Mars. Science (accepted).

Fries, M., et al., 2022. The SHERLOC Calibration Target on the Mars 2020 Perseverance Rover: Design, Operations, and Extended Outreach Functions. Space Science Reviews.

Fu, X., Wang, A., Krawczynski, M.J., 2017. Characterizing amorphous silicates in extraterrestrial materials: polymerization effects on Raman and mid-IR spectral features of alkali and alkali earth silicate glasses. J. Geophys. Res. Planets 122 (5), 839–855. https://doi.org/10.1002/2016JE005241.

Goudge, T.A., Mustard, J.F., Head, J.W., Fassett, C.I., Wiseman, S.M., 2015. Assessing the mineralogy of the watershed and fan deposits of the Jezero crater paleolake system, Mars. J. Geophys. Res. Planets. 120, 775–808.

Goudge, T.A., Milliken, R.E., Head, J.W., Mustard, J.F., Fassett, C.I., 2017. Sedimentological evidence for a deltaic origin of the western fan deposit in Jezero crater, Mars and implications for future exploration. Earth Planet. Sci. Lett. 458, 357–365.

Goudge, T.A., Mohrig, D., Cardenas, B.T., Hughes, C.M., Fassett, C.I., 2018. Stratigraphy and paleohydrology of delta channel deposits, Jezero crater, Mars. Icarus 301, 58–75.

Horgan, B.H.N., Anderson, R.B., Dromart, G., Amador, E.S., Rice, M.S., 2020. The mineral diversity of Jezero crater: evidence for possible lacustrine carbonates on Mars. Icarus 339, 113526.

Kuebler, K.E., Jolliff, B.L., Wang, A., Haskin, L.A., 2006. Extracting olivine (Fo-Fa) compositions from Raman spectral peak positions. Geochim. Cosmochim. Acta 70 (24), 6201–6222. https://doi.org/10.1016/j.gca.2006.07.035.

Leutenegger, S., et al., 2011. BRISK: Binary robust invariant scalable keypoints. In: 2011 International Conference on Computer Vision, pp. 2548–2555.

Liu, Y., et al., . A ferroan olivine cumulate on the floor of Jezero crater, Mars. Sci. Adv. (in review).

Mandon, L., Quantin-Nataf, C., Thollot, P., Mangold, N., Lozac'h, L., Dromart, G., Beck, P., Dehouck, E., Breton, S., Millot, C., Volat, M., 2020. Refining the age, emplacement and alteration scenarios of the olivine-rich unit in the Nili fossae region, Mars. Icarus 336, 113436.

Mangold, N., Dromart, G., Ansan, V., Salese, F., Kleinhans, M.G., Massé, M., Quantin-Nataf, C., Stack, K.M., 2020. Fluvial regimes, morphometry, and age of Jezero crater Paleolake inlet valleys and their exobiological significance for the 2020 rover Mission landing site. Astrobiology 20, 994–1013.

Mangold, N., Gupta, S., Gasnault, O., Dromart, G., Tarnas, J.D., Sholes, S.F., Horgan, B., Quantin-Nataf, C., Brown, A.J., Le Mouélic, S., Yingst, R.A., Bell, J.F., Beyssac, O., Bosak, T., Calef, F., Ehlmann, B.L., Farley, K.A., Grotzinger, J.P., Hickman-Lewis, K., Holm-Alwmark, S., Kah, L.C., Martinez-Frias, J., McLennan, S.M., Maurice, S., Nuñez, J.I., Ollila, A.M., Pilleri, P., Rice, J.W., Rice, M., Simon, J.I., Shuster, D.L., Stack, K.M., Sun, V.Z., Treiman, A.H., Weiss, B.P., Wiens, R.C., Williams, A.J., Williams, N.R., Williford, K.H., 2021. Perseverance rover reveals an ancient delta-lake system and flood deposits at Jezero crater. Mar. Sci. 374, 711–717.

Moeller, R.C., Jandura, L., Rosette, K., Robinson, M., Samuels, J., Silverman, M., Brown, K., Duffy, E., Yazzie, A., Jens, E., Brockie, I., White, L., Goreva, Y., Zorn, T., Okon, A., Lin, J., Frost, M., Collins, C., Williams, J.B., et al., 2020. The sampling and caching subsystem (SCS) for the scientific exploration of Jezero crater by the Mars 2020 perseverance rover. Space Sci. Rev. 217 (1), 5. https://doi.org/10.1007/s11214-020-00783-7.

Mysen, B.O., Finger, L.W., Virgo, D., Seifert, F.A., 1982. Curve-fitting of Raman spectra of silicate glasses. Am. Mineral. 67, 686–695.

Razzell Hollis, J., Abbey, W., Beegle, L.W., Bhartia, R., Ehlmann, B.L., Miura, J., Monacelli, B., Moore, K., Nordman, A.D., Scheller, E.L., Uckert, K., Wu, Y.-H., 2021. A deep-ultraviolet Raman and fluorescence spectral library of 62 minerals for the SHERLOC instrument onboard Mars 2020. Planet. Space Sci. 209 (May), 105356 https://doi.org/10.1016/j.pss.2021.105356.

Razzell Hollis, J., Sharma, S., Abbey, W., Bhartia, R., Beegle, L.W., Fries, M., Hein, J.D., Monacelli, B., Nordman, A.D., 2022. A deep-ultraviolet Raman and fluorescence spectral library of 51 organic compounds for the SHERLOC instrument onboard Mars 2020. Astrobiology (accepted).

Rull, F., Martinez-Frias, J., Sansano, A., Medina, J., Edwards, H.G.M., 2004. Comparative micro-Raman study of the Nakhla and Vaca Muerta meteorites. J. Raman Spectrosc. 35 (6), 497–503. https://doi.org/10.1002/jrs.1177.

Scheller, E.L., Razzell Hollis, J., Cardarelli, E., Steele, A., Beegle, L.W., Bhartia, R., Conrad, P., Uckert, K., Sharma, S., Ehlmann, B.L., et al., 2022. Aqueous alteration processes and implications for organic geochemistry in Jezero crater, Mars. Science (accepted).

Schon, S.C., Head, J.W., Fassett, C.I., 2012. An overfilled lacustrine system and progradational delta in Jezero crater, Mars: implications for Noachian climate. Planet. Space Sci. 67, 28–45.

Shkolyar, S., Farmer, J.D., 2018. Biosignature preservation potential in playa evaporites: impacts of diagenesis and implications for Mars exploration. Astrobiology 18 (11), 1460–1478. https://doi.org/10.1089/ast.2018.1849.

Shkolyar, S., Eshelman, E.J., Farmer, J.D., Hamilton, D., Daly, M.G., Youngbull, C., 2018. Detecting kerogen as a biosignature using colocated UV time-gated Raman and fluorescence spectroscopy. Astrobiology 18 (4), 431–454. https://doi.org/10.1089/ast.2017.1716.

Stack, K.M., Williams, N.R., Calef, F., Sun, V.Z., Williford, K.H., Farley, K.A., Eide, S., Flannery, D., Hughes, C., Jacob, S.R., Kah, L.C., Meyen, F., Molina, A., Nataf, C.Q., Rice, M., Russell, P., Scheller, E., Seeger, C.H., Abbey, W.J., Adler, J.B., Amundsen, H., Anderson, R.B., Angel, S.M., Arana, G., Atkins, J., Barrington, M., Berger, T., Borden, R., Boring, B., Brown, A., Carrier, B.L., Conrad, P., Dypvik, H., Fagents, S.A., Gallegos, Z.E., Garczynski, B., Golder, K., Gomez, F., Goreva, Y., Gupta, S., Hamran, S.-E., Hicks, T., Hinterman, E.D., Horgan, B.N., Hurowitz, J., Johnson, J.R., Lasue, J., Kronyak, R.E., Liu, Y., Madariaga, J.M., Mangold, N., McClean, J., Miklusicak, N., Nunes, D., Rojas, C., Runyon, K., Schmitz, N., Scudder, N., Shaver, E., SooHoo, J., Spaulding, R., Stanish, E., Tamppari, L.K., Tice, M.M., Turenne, N., Willis, P.A., Aileen Yingst, R., 2020. Photogeologic map of the perseverance rover field site in Jezero crater constructed by the Mars 2020 science team. Space Sci. Rev. 216, 127.

Sutter, B., McAdam, A.C., Mahaffy, P.R., Ming, D.W., Edgett, K.S., Rampe, E.B., Eigenbrode, J.L., Franz, H.B., Freissinet, C., Grotzinger, J.P., Steele, A., House, C.H., Archer, P.D., Malespin, C.A., Navarro-González, R., Stern, J.C., Bell, J.F., Calef, F.J., Gellert, R., Glavin, D.P., Thompson, L.M., Yen, A.S., 2017. Evolved gas analyses of sedimentary rocks and eolian sediment in Gale crater, Mars: results of the curiosity rover's sample analysis at Mars instrument from Yellowknife Bay to the Namib dune. J. Geophys. Res. 122, 2574–2609.

Tanaka, R., Yuge, K., Kawai, J., Alawadhi, H., 2017. Artificial peaks in energy dispersive X-ray spectra: sum peaks, escape peaks, and diffraction peaks. X-Ray Spectrom. 46, 5–11.

Thomas, N.H., Ehlmann, B.L., Meslin, P.Y., Rapin, W., Anderson, D.E., Rivera-Hernandez, F., Forni, O., Schroder, S., Cousin, A., Mangold, N., Gellert, R., Gasnault, O., Wiens, R.C., 2019. Mars science laboratory observations of chlorine salts in Gale crater, Mars. Geophysical Research Letters 46 (10), 10754–10763.

Tice, M.M., et al., 2022. Primary and alteration textures of Séítah formation rocks inferred by PIXL X-ray fluorescence, X-ray diffraction, and multispectral imaging on Mars. Sci. Adv. (in review).

Uckert, K., Bhartia, R., Michel, J., 2019. A semi-autonomous method to detect cosmic rays in Raman hyperspectral data sets. Appl. Spectrosc. 73 (9), 1019–1027. https://doi.org/10.1177/0003702819850584.

Uckert, K., Bhartia, R., Beegle, L.W., Monacelli, B., Asher, S.A., Burton, A.S., Bykov, S.V., Davis, K., Fries, M.D., Jakubek, R.S., Razzell Hollis, J., Roppel, R.D., Wu, Y.-H., 2021. Calibration of the SHERLOC deep ultraviolet fluorescence–raman spectrometer on the Perseverance Rover. Appl. Spectrosc. 75 (7), 763–773. https://doi.org/10.1177/00037028211013368.

Williford, K.H., Farley, K.A., Stack, K.M., Allwood, A.C., Beaty, D., Beegle, L.W., Bhartia, R., Brown, A.J., de la Torre Juarez, M., Hamran, S.-E., Hecht, M.H., Hurowitz, J.A., Rodriguez-Manfredi, J.A., Maurice, S., Milkovich, S., Wiens, R.C., 2018. In: Cabrol, N.A., Grin, E.A. (Eds.), From Habitability to Life on Mars. Elsevier, pp. 275–308 https://www.sciencedirect.com/science/article/pii/B9780128099353000104.